Monthly Notices of the ROYAL ASTRONOMICAL SOCIETY

MNRAS **520,** 437–445 (2023) https://doi.org/10.1093/mnras/stad104
Advance Access publication 2023 January 13

Multi-spacecraft observations of shocklets at an interplanetary shock

D. Trotta [1]★ H. Hietala,[1,2] T. Horbury [1] N. Dresing,[3] R. Vainio,[3] L. Wilson, III,[4] I. Plotnikov[5] and E. Kilpua[6]

[1]*The Blackett Laboratory, Department of Physics, Imperial College London, London SW1234, UK*
[2]*School of Physics and Astronomy, Queen Mary University of London, London E1 4NS, UK*
[3]*Department of Physics and Astronomy, University of Turku, FI-20014 Turku, Finland*
[4]*NASA Goddard Space Flight Center, Greenbelt, MD 20771, USA*
[5]*IRAP, Université Toulouse III – Paul Sabatier, CNRS, CNES, F-31062 Toulouse, France*
[6]*Department of Physics, University of Helsinki, FI-00014 Helsinki, Finland*

Accepted 2023 January 5. Received 2022 December 7; in original form 2022 September 27

ABSTRACT

Interplanetary (IP) shocks are fundamental building blocks of the heliosphere, and the possibility to observe them *in situ* is crucial to address important aspects of energy conversion for a variety of astrophysical systems. Steepened waves known as shocklets are known to be important structures of planetary bow shocks, but they are very rarely observed related to IP shocks. We present here the first multi-spacecraft observations of shocklets observed by upstream of an unusually strong IP shock observed on 3 November 2021 by several spacecraft at L1 and near-Earth solar wind. The same shock was detected also by radially aligned Solar Orbiter at 0.8 AU from the Sun, but no shocklets were identified from its data, introducing the possibility to study the environment in which shocklets developed. The Wind spacecraft has been used to characterize the shocklets, associated with pre-conditioning of the shock upstream by decelerating incoming plasma in the shock normal direction. Finally, using the Wind observations together with ACE and DSCOVR spacecraft at L1, as well as THEMIS B and THEMIS C in the near-Earth solar wind, the portion of interplanetary space filled with shocklets is addressed, and a lower limit for its extent is estimated to be of about $110R_E$ in the shock normal direction and $25R_E$ in the directions transverse to the shock normal. Using multiple spacecraft also reveals that for this strong IP shock, shocklets are observed for a large range of local obliquity estimates (9°–64°).

Key words: plasmas – shock waves – waves.

1 INTRODUCTION

Shocks are ubiquitous, and they are fundamental for a broad range of astrophysical systems (e.g. Kivelson & Russell 1995; Bykov et al. 2019). Generally speaking, shocks convert directed flow energy (upstream) into heat and magnetic energy (downstream) and, in the collisionless case, in energetic particles (e.g. Burgess & Scholer 2015).

Interplanetary (IP) shocks, found in the heliosphere, are generated as a consequence of solar phenomena, such as Coronal Mass Ejections (CME) and Stream Interaction Regions (SIR; Dessler & Fejer 1963; Gosling et al. 1974; Kilpua, Koskinen & Pulkkinen 2017; Richardson 2018). IP shocks play an important role for the overall heliosphere energetics, due to their ability to accelerate particles to high energies and modify the plasma environments in their surroundings (see Reames 1999, for a review). Furthermore, IP shocks provide a unique opportunity for *in situ* observations using the the instrumentation on board of spacecraft, a mean of analysis inaccessible in astrophysical shocks. Another group of shocks routinely observed in the heliosphere are the planetary bow shocks, resulting from the interaction between the supersonic solar wind and the planets that behave as obstacles (Hoppe & Russell 1982). From this point of view, the Earth's bow shock has become a prototype for studying various phenomena characterized by the presence of shocks, due to the convenience to be probed, starting from the early *Pioneer* evidences (Dungey 1979) to the modern spacecraft observations such as the Magnetospheric MultiScale (MMS) mission (Burch et al. 2016).Generally speaking, IP shocks are weaker and show larger radii of curvature with respect to planetary bow shocks, a feature inducing several differences in their upstream/downstream plasma environments (e.g. Eastwood et al. 2015; Kilpua et al. 2015; Dresing et al. 2016; Wilson 2016).

The shock structure and behaviour is regulated by several parameters, one of the most important of which is the angle between the shock normal direction and the upstream magnetic field, θ_{Bn}. When θ_{Bn} is close to 90°, the shock is quasi-perpendicular. On the other hand, for θ_{Bn} values close to 0° (corresponding to an upstream magnetic field almost normal to the shock surface), the shock is quasi-parallel. Other important parameters for the shock behaviour are the shock Alfvénic and fast magnetosonic Mach numbers, i.e. the ratio between the shock speed in the upstream flow frame and the upstream Alfvén and fast magnetosonic speed, respectively (M_A

★ E-mail: d.trotta@imperial.ac.uk

$\equiv v_{sh}/v_A$ and $M_{fms} \equiv v_{sh}/v_{fms}$). Finally, another important parameter to address shock behaviour is the plasma beta, defined as the ratio between thermal and magnetic energy densities and often expressed as a ratio between thermal and Alfvén speeds $\beta \equiv v_{th}^2/v_A^2$. Particle reflection and subsequent propagation far upstream is favoured at high Mach number (super-critical) quasi-parallel shocks (Kennel, Edmiston & Hada 1985). This introduces the possibility for reflected particles to interact with the upstream plasma over long distances, creating unstable distributions and a collection of disturbances in the plasma properties. This region of interaction between the shock and its upstream is called the foreshock, and it is fundamental for many aspects of energy conversion in collisionless plasmas (Wilson 2016).

Shock-reflected, energetic ions are also thought to be responsible for the emergence of steepened waves in the shock upstream. These steep structures, that are observed to shave short (< 1 min) duration, are called shocklets and Short Large Amplitude Magnetic Structures (SLAMS) depending on their typical signatures, and are both characterized by steep, strong enhancements of the magnetic field magnitude (e.g. Stasiewicz et al. 2003; Plaschke et al. 2018). Shocklets are likely to play an important role for particle acceleration at quasi-parallel shocks, due to their ability to induce effective pre-conditioning of incoming plasma before its interaction with the shock (e.g. Wilson et al. 2013). Furthermore, particle acceleration up to energies of about 100 keV due to shocklets has recently been found upstream of the Earth's bow shock (Stasiewicz et al. 2021). Despite many observational (e.g. Lucek et al. 2008) and theoretical (e.g. Hellinger, Mangeney & Matthews 1996; Scholer, Kucharek & Shinohara 2003) efforts, the (non-linear) mechanisms leading to the formation of shocklets are still a matter of debate. The emerging picture is that shocklets are created in consequence of ultra-low-frequency (ULF) foreshock waves (see Lucek et al. 2002; Lucek et al. 2008; Wilson 2016). Recently, a comprehensive study about the role of the counterstreaming ion beam instability for shocklet formation and growth by Stasiewicz & Klos (2022), looking at a quasi-parallel Earth's bow shock crossing by MMS.

Despite the mystery surrounding their formation mechanisms, shocklets have been observed *in situ* for a large variety of shocks. These include the planetary bow shocks of Earth (e.g. Russell, Childers & Coleman Jr 1971), Jupiter (Tsurutani et al. 1993), and Saturn (Bertucci et al. 2007; Andrés et al. 2013), as well as the cometary bow shocks of the Giacobini–Zinner (Thomsen et al. 1986; Tsurutani et al. 1987), Halley (Naeem et al. 2020), and Grigg–Skjllerup (Coates, Mazelle & Neubauer 1997).

Most of the knowledge about shocklets is due to observations at planetary bow shocks. Shocklets are characterized by an upstream sharp leading edge followed by a slower relaxation (e.g. Lucek et al. 2002). Furthermore, it has been found that shocklets are often associated with whistler wave precursors (Hoppe et al. 1981) unstable electron distributions (Wilson et al. 2009). Importantly, all shocklet observations show diffuse ion distributions (e.g. Hoppe & Russell 1983), which likely represent an important ingredient for efficient wave steepening, as shown by early simulation works (e.g. Omidi & Winske 1990). The typical duration of shocklets is of about 30 s at the Earth's bow shock (Wilson 2016). It may also be noted that shocklets are often defined as having weak magnetic compression $\delta B/B_0 \lesssim 2$, while, for SLAMS, the requirement $\delta B/B_0 \gtrsim 2$ is used (see e.g. Plaschke et al. 2018).

At IP shocks, shocklets observations are much more rare than planetary bow shocks, making the few available observations of particular interest, as they yield to a better understanding of the origin and evolution of these phenomena. The first of these observations is due to Lucek & Balogh (1997), who reported the presence of a structure in the magnetic field measured by the *Ulysses* spacecraft (Balogh et al. 1995) upstream of a quasi-parallel interplanetary shock on 6 January 1992, with features similar to shocklets observed at Earth's bow shock by Le et al. (1992), with the difference of being associated with whistler precursor. Unfortunately, this observation was limited by the fact that only magnetic field data were available, leaving the plasma properties around the structure out of reach. More than a decade later, using the Wind spacecraft data, Wilson et al. (2009) reported the presence of 12 shocklets upstream of the quasi-perpencdicular, high Mach number IP shock of 6 April 2000. This event, labelled by the authors 'the unusual event' (with respect to more than 400 other IP shocks observed by Wind), is the second (and last before this work, to the best of our knowledge) shocklet observation at IP shocks. To make the 6 April 2000 event even more interesting is the fact that the local θ_{Bn} of the shock was estimated to be of 68°, and so less likely to have upstream conditions favourable for wave steepening.

In this work, we present the first multi-spacecraft observations of IP shock shocklets (seen by several spacecraft near Earth), enabling us to investigate the spatial and temporal transient nature of such steep waves. Furthermore, the same shock is observed by Solar Orbiter, well aligned radially and ∼ 3500 Earth radii upstream of Earth. At Solar Orbiter, no shocklets are found, making it possible to study the environment in which upstream wave steepening happened.

This paper is organized as follows: Section 2 presents the spacecraft data products employed in this work (Section 2.1) and the techniques used for shock parameter estimation and shocklet characterization (Section 2.2); the spacecraft observations are presented in Section 3, with an overview of the event shown in Section 3.1; the detailed shocklet observations are presented in Section 3.2, and the multi-spacecraft observations of such structures are then presented in Section 3.3; this paper ends with the conclusions reported in Section 4.

2 DATA AND METHODS

2.1 *In situ* measurements

Throughout this study, magnetic field and plasma data from several spacecraft have been used. At Solar Orbiter, the magnetic field has been measured with a resolution of 64 vectors/s by the flux-gate magnetometer MAG (Horbury et al. 2020), while ion bulk flow, density, and temperature are the ground computed plasma moments measured by the Solar Wind Analyser (SWA) suite (Owen et al. 2020), with a 4-s resolution.

For the Wind data shown (Wilson et al. 2021), the magnetic field is measured using the Wind Magnetic Field Investigation (MFI), at a resolution of 11 vectors/s (Lepping et al. 1995), and the ion moments are obtained using the Wind Three-Dimensional Plasma and Energetic Particle Investigation (3DP) instrument at 3-s resolution (Lin et al. 1995). The measurements obtained with the 3DP instrument are consistent with those obtained with the Solar Wind Experiment instrument (Ogilvie et al. 1995). A collection of other spacecraft has been used near Earth, in particular: the Advanced Composition Explorer (ACE) magnetic field experiment at 1-s resolution (Smith et al. 1998), the Deep Space Climate Observatory (DSCOVR) magnetometer at 1-s resolution (Szabo et al. 2016), and the THEMIS B and C Flux Gate Magnetometer (FGM; Auster et al. 2008) and electrostatic analyser (ESA McFadden et al. 2008) at 4-s resolution. The high resolution provided by

Table 1. Shock arrival time and parameters computed for different spacecraft.

Spacecraft	GSE position (R_E)	Shock time (UT)	$\langle \hat{n}_{GSE} \rangle$	$\langle \theta_{Bn} \rangle$ (°)	$\langle r_B \rangle$	$\langle r \rangle$	$\langle v_{sh} \rangle$	β_{up}	M_{fms}	M_A
Solar Orbiter	[3482.9, 283.9. −744.8]	14:04:26	[−0.51, 0.49, −0.71]	45.3	2.62	1.47	691.8	0.5	5.5	6.2
Wind	[196.5, 14.3, −10.5]	19:35:01	[−0.87, −0.04, −0.49]	33.1	3.10	5.15	768.8	0.4	5.3	5.6
ACE	[230.9, −40.0, 12.49]	19:24:05	[−0.67, 0.33, −0.66]	9.6	1.93	–	–	–	–	–
DSCOVR	[240.2, 30.9, 25.5]	19:24:50	[−0.67, 0.03, −0.74]	13.3	2.83	–	–	–	–	–
THB	[52.9, −12.8, 2.8]	19:43:20	[−0.79, −0.01, −0.61]	50.1	2.06	2.93	625.9	–	–	5.8
THC	[54.7, −15.7, 2.9]	19:43:30	[−0.79, 0.01, −0.61]	64	1.2	1.54	686.1	–	–	6.4

Notes. The parameters shown are (left to right): shock normal vector, θ_{Bn}, magnetic compression ratio r_B, gas compression ratio r, shock speed v_{sh}, upstream plasma beta β_{up}, fast magnetosonic and Alfvénic Mach numbers (M_{fms} and M_A, respectively). The shock normals are shown in the GSE frame of reference, with θ_{Bn} expressed in degrees. The shock speed v_{sh} in the spacecraft frame is expressed in km s^{-1} and it is aligned to the shock normal.

Wind data has been used to investigate the fine details of shocklets (including their high-frequency wave precursors), as discussed below.

2.2 Shock parameter estimation and shocklet characterization

The shock normal (and therefore the θ_{Bn}) estimation is done using the Mixed Mode 3 method (MX3; see Paschmann & Schwartz 2000) for Solar Orbiter, Wind and THEMIS B and C. The results obtained with the other mixed modes are compatible with the ones shown here. When plasma data for the event is not available (as in the case of DSCOVR and ACE), the magnetic coplanarity method is used to determine the shock normal vector. The shock speed is computed through the mass flux conservation, and it is along the shock normal, in the spacecraft frame. Such techniques for shock parameter estimation have been extensively used and discussed in previous literature (e.g. Koval & Szabo 2008). Given the nature of such techniques, care has been taken to choose appropriate time intervals to define upstream and downstream of the shock at each observation. For all the parameters computed and presented here, the averaging $\langle\rangle$ indicates that different upstream/downstream windows have been used systematically, to make sure that the parameters estimation is robust. Here, we used a range of upstream/downstream averaging windows lasting in a range between ∼30 s and 5 min. Further information about the properties and importance of this systematic way of computing shock parameters starting from a single spacecraft crossing signal can be found in Trotta et al. (2022a).

A summary of the parameters estimated for each spacecraft crossing can be found in Table 1. As it will be discussed in detail below, the shock appears to have an unusually high Mach number, a key property to address its behaviour. Furthermore, with reference to Table 1, we note that the parameter estimation at THB and THC is the most sensitive to the choice of upstream and downstream windows, due to the strong structuring of the shock transition and the resolution available for the measurements. The parameter estimation involving temperature measurements for the THEMIS B and C spacecraft have been discarded here, due to the fact that such measurements are known to overestimate ion temperature in the solar wind, when the spacecraft are in magnetospheric mode.

Another important part of the methods used in this work has to do with shocklet identification. Here, shocklets are identified by visual inspection as steep enhancements of magnetic field with an upstream sharp leading edge followed by a slower relaxation, following the definition in Wilson (2016). In the absence of a more formal definition of shocklet structure accepted by the literature, throughout this work, we identify them by visual inspection, looking for the features discussed above (see Section 1).

3 SPACECRAFT OBSERVATIONS

3.1 Event Overview

On 3 November 2021, a fast-forward, CME-driven IP shock reached Solar Orbiter. Later on, the shock was observed by several other spacecraft near the Earth. Table 1 shows the shock arrival time and key parameters as observed by the Solar Orbiter, Wind, DSCOVR, ACE, THEMIS B, and THEMIS C (columns).

Given the large number of satellites observing this shock, we checked if the high shock speeds computed using local upstream and downstream averaging windows and the mass flux algorithm are compatible with multiple spacecraft timing techniques. To this end, the shock speed was estimated using the local shock normals and using a two-spacecraft timing, as well as with a four-spacecraft timing technique using the near-Earth spacecraft (see Paschmann & Schwartz 2000, for details). These estimations are compatible with what we found using the mass flux algorithm, but yield to a large spread of values with $450 \lesssim v_{sh} \lesssim 1100$ km s^{-1}, suggesting that the assumption of shock planarity may not be well suited for this event. Other effects responsible for this large spread of values may be related to rotation, curvature, and mass-loading effects.

The top panel of Fig. 1 shows an overview of the Sun–Earth system, including the position of Solar Orbiter, obtained using the Solar MAgnetic Connection HAUS tool (Solar-MACH) software (Gieseler 2022). Here, the dashed lines show the radial connection between Solar Orbiter (the Earth) and the Sun, while the solid lines represent the connections through the Parker spiral. It can be noted that Solar Orbiter is well radially-aligned to Earth (and L1), making it a relevant configuration for multi-spacecraft studies.

This interesting alignment has been put in the context on the IP shock passage in the bottom panel of Fig. 1. Here, the positions of Solar Orbiter, Wind, THEMIS B, and ACE are shown in the three-dimensional space in GSE coordinates (diamonds). Superimposed to the spacecraft position are the shock normal vectors, computed as described in Section 2.2. The dark arrows represent the average shock normal vectors. It is possible to note that the normals computed for the spacecraft at L1 have some degree of fluctuation, probably due to shock front irregularities, a typical feature of high Mach number, super-critical shocks (e.g. Johlander et al. 2016; Trotta & Burgess 2018; Kajdič et al. 2019; Preisser et al. 2020). Shock front irregularities may also be induced by pre-existing turbulence, as elucidated by recent studies (Guo, Giacalone & Zhao 2021; Trotta et al. 2021, 2022b; Nakanotani, Zank & Zhao 2022). The parameter estimation in Table 1 is consistent with such irregularities.

To further characterize the strong variability of this shock transition, we studied the angle between the magnetic field and plasma flow in the spacecraft reference frame in the shock upstream, $\langle \theta_{UB} \rangle_{Upstream}$. This parameter is an indicator of the shock behaviour, as quasi-

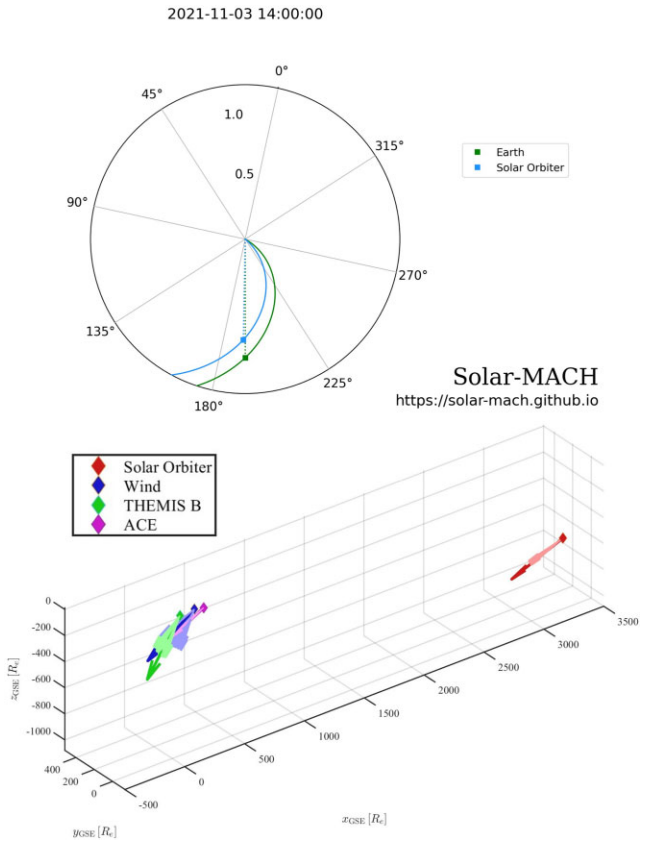

Figure 1. Top panel: Spacecraft configuration at 14:00 on 3 November 2021. The Sun is at the centre of the plot, with radial and magnetic field connections to Solar Orbiter and Earth represented by dotted and solid lines, respectively. Bottom panel: three-dimensional overview of the Solar Orbiter, Wind, THEMIS B, and ACE spacecraft relative positions (points). Earth is located in (0,0,0). Superimposed are the shock normals computed using different averaging windows for each spacecraft, and their mean (light and dark arrows, respectively).

parallel flow of solar wind facilitates ion–ion counter streaming instabilities which lead to the formation of shocklets. Using averaging windows between 5 and 20 min in the immediate shock upstream (up to 30 s before the shock crossing), we found $\langle\theta_{UB}\rangle_{Upstream}$ to be of 68° at Solar Orbiter, while $\langle\theta_{UB}\rangle_{Upstream} \sim 38°$ at Wind. This difference implies that ion–ion streaming instabilities are favoured at Wind, an important ingredient for shocklets formation.

Fig. 2 shows the *in situ* observations of the 3 November IP shock as seen by Solar Orbiter (left-hand panel) and Wind (right-hand panel). As shown in Table 1, the observed shock parameters indicate that we are in presence of a shock with a θ_{Bn} that has strong local variations ($9 \lesssim \theta_{Bn} \lesssim 64$). The shock has unusually high Mach numbers ($M_{fms} \sim 5$, $M_A \sim 6$) with respect to other IP shocks (see Kilpua et al. 2015, for example).

The IP shock crossed the Wind spacecraft around 19:35. For this crossing, the local estimation of the shock normal vector using magnetic coplanarity and mixed modes are all consistent, and indicate a low θ_{Bn} value (of about 33°). These Wind observations are shown on the right hand side panels of Fig. 2. The magnetic field observed by Wind shows very extended structuring over a broad range of scales both upstream and downstream, consistent with the quasi-parallel geometry inferred for the shock (e.g. Blanco-Cano et al. 2016). The fast magnetosonic and Alfvénic Mach numbers are high also at Wind (5.3 and 5.6, respectively). For this event, we observe a very small value for the upstream proton density (about 2 particles per cm^{-3}, a value consistent for both the 3DP and SWE experiment on-board the spacecraft), with the gas compression ratio exceeding the MHD limiting value of 4 (with $\langle r\rangle \sim 5.15$). An extended range of fluctuations is also observed for the plasma moments, as expected for this strong shock. The ion density and temperature increase sharply upon the shock arrival, and are modulated by the large-scale downstream fluctuations. At Wind, temperature is much higher than at Solar Orbiter, and vice-versa for the density. This feature is interesting, especially as the spacecraft are well-aligned radially. To investigate the reasons for such a behaviour is beyond the scope here and will be object of further investigation.

The IP shock had crossed Solar Orbiter at 14:04 of the same day. The overview plot on the left-hand side of Fig. 2 shows several interesting features. First of all, the magnetic field upstream of the shock reveals structuring over a broad range of frequencies, as we discuss in detail below. Particularly interesting is the discontinuity observed at around 12:30, associated with a slight increase of ion temperature upstream of the shock, and possibly a pre-conditioning of the incoming particle population. Another interesting feature of this IP shock crossing is related to the ion density increase observed by Solar Orbiter, which is not sharply rising at the time corresponding to the shock arrival, but instead grows smoothly deeper downstream, yielding a small value for the local (i.e. using averaging windows of order of 1-min duration) evaluation of the gas compression ratio $\langle r\rangle \sim 1.47$, while the magnetic compression ratio is larger ($\langle\langle r_B\rangle \sim 2.62$). Compression ratios show significant variations at each spacecraft, consistent with the high level of fluctuations observed for this shock. Finally, we note that the ion temperature increase observed at Solar Orbiter is rather small, with the temperature starting to rise a few minutes before the shock passage, probably due to shock-produced reflected particles injected upstream. Further properties of the shock, including the flux rope identified (not shown here) in the immediate shock downstream (and seen deeper in the shock downstream at Wind; not shown), are also interesting but beyond the scope of this paper.

3.2 Shocklets at Wind

In this section, the details of upstream shocklets are addressed using the Wind data that have the highest cadence in magnetic field and plasma available data among the spacecraft that observe upstream shocklets. The 30-min upstream of the IP shock observed by Wind are characterized by the presence of several shocklets. Such structures can be clearly observed in the top panel of Fig. 3, and are often associated with high-frequency wave trains upstream their leading edges, as shown in Fig. 4. The most evident shocklets have been highlighted in Fig. 3 with orange-shaded panels.

In panel (b) of Fig. 3, we show the proton bulk flow speed along the shock normal, in the shock frame $U_n^{sh} \equiv \mathbf{U} \cdot \hat{n} - v_{sh}$. We observe that the shocklets are associated with an effective deceleration of the upstream plasma, as it can be seen from the spikes in U_n^{sh} (the clearest of them is highlighted by the black arrows in Fig. 3). The noise level is higher for the proton density and temperature signals (panels c–d); however, it is possible to see that plasma compression and heating associated with shocklets is resolved for some of them.

Upstream shocklets are further investigated in Fig. 4. Here, we show two examples of such structures in the shock upstream and highlight their details. These shocklets are highlighted by the black arrows in the overview Fig. 3. Panels (a) and (b) of the Figure show zooms over ∼ 8-min intervals of magnetic field magnitude and

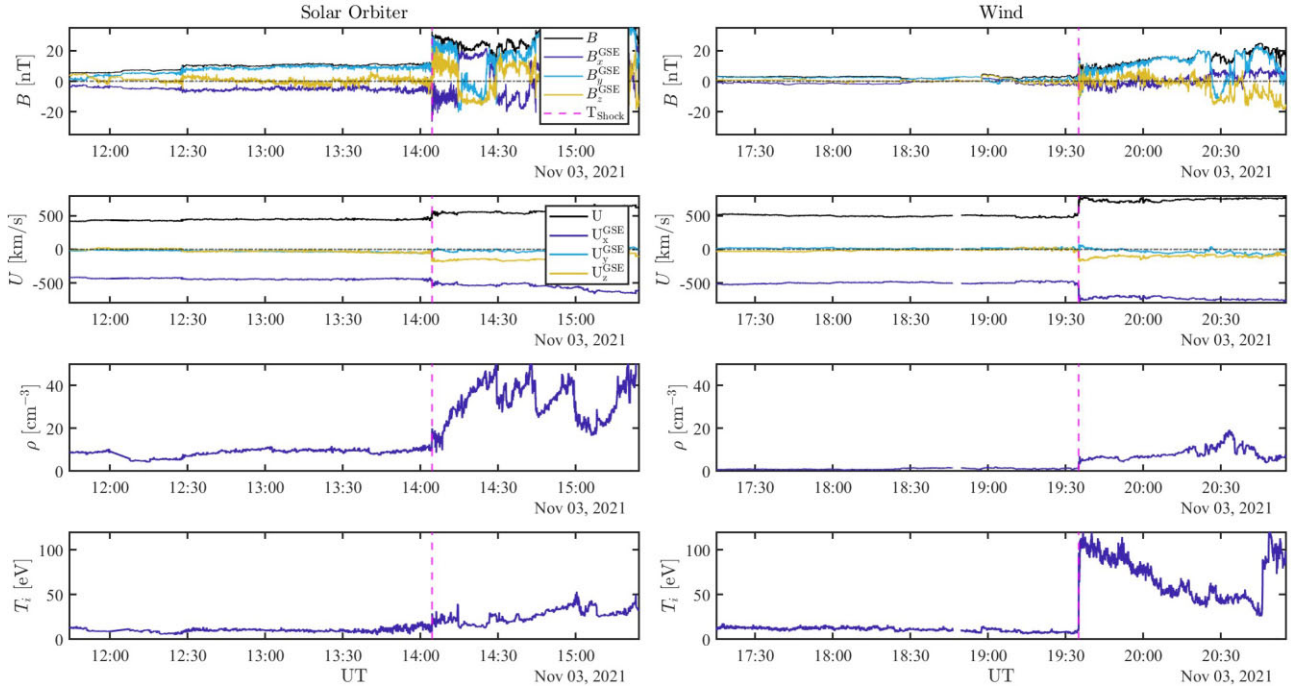

Figure 2. Magnetic field magnitude and components, ground-computed ion bulk flow speed, ion density, ion temperature (top to bottom) for the IP shock observed first by Solar Orbiter (left-hand panel) and later by Wind (right-hand panel).

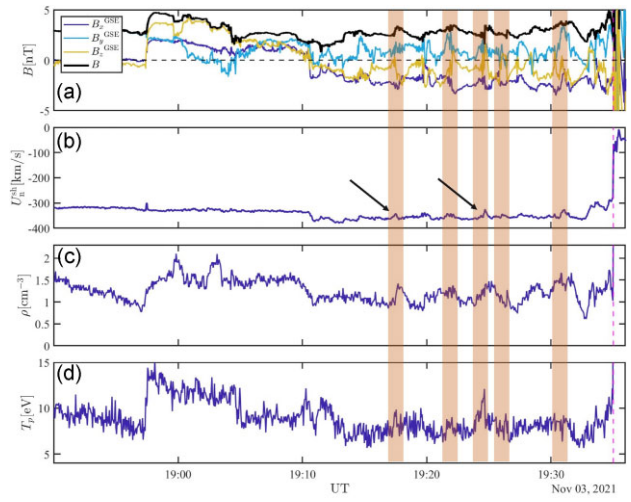

Figure 3. The shock upstream observed by the Wind spacecraft. From top to bottom: magnetic field magnitude (black) and its components in the GSE coordinate system (colors), ion bulk flow speed normal to the shock, in the shock rest frame, proton density, and temperature observed by the Wind-3DP instrument. The arrows mark the upstream proton bulk flow speed deceleration correspondent to two of the most clear shocklets, discussed in detail in Fig. 4. The dashed magenta line marks the shock arrival.

components (solid lines) around two shocklets. The vertical red line marks the upper half of the leading edge of the shocklet. We can see important differences between the Shocklet 1 and Shocklet 2. First of all, Shocklet 2 has a much sharper leading edge (with a rise time, i.e. the time between the backgorund upstream magnetic field value and its peak, of about 4 s), and shows strong structuring, including a well-developed high-frequency wave train in the shocklet upstream and an overshoot/unsdershoot feature (immediately after the red line in Fig. 4b) in the relaxation phase. On the other hand, Shocklet 1 is characterized by a a larger rise time ($\sim$ 10 s) and less prominent structuring, with shorter high-frequency wave packet upstream and a smoother relaxation phase ($\sim$ 90 s). We infer that, since Shocklet 1 is upstream of Shocklet 2, the former is still in the early phase of the process of steepening, and Shocklet 2 has evolved further. Such a consideration about the different stages in the structures' evolution, considering the fact that they are observed to be extremely close to each other ($\sim$ 10 min, corresponding to about 30 proton cyclotron times $T_{cp} \equiv 1/f_{cp}$, where f_{cp} is the proton cyclotron frequency computed using the mean value for the upstream magnetic field of 3 nT) highlights their transient nature.

The high-frequency wave precursors have been highlighted with the green shaded areas in panels (a) and (b) of Fig. 4. To further investigate the nature of these precursors, we performed a Minimum Variance Analysis (MVA; Paschmann & Schwartz 2000) over the highlighted intervals. In these intervals, the intermediate to minimum eigenvalue ratio λ_2/λ_3 for the MVA matrix is large, with $\lambda_2/\lambda_3 \sim$ 15, 65 for Shocklet 1 and 2, respectively. A larger value of these ratios can be achieved filtering the data (Wilson et al. 2017). The magnetic field components are projected to the minimum variance frame and shown in panels (c)–(e) of Fig. 4. Here, it can be seen that the waves in the precursor have periods of about 2 s. Finally, panels (d)–(f) of the figure show hodograms for the intermediate and maximum variance magnetic field, showing that they are circularly right-hand polarized in the spacecraft frame. This is expected for whistler wave modes, and it is indicative of the dispersive nature of shocklets, consistent with other studies (e.g. Hoppe et al. 1981; Wilson et al. 2009). Note that these modes are often seen as left-handed in the terrestrial foreshock since they are trying to propagate against the solar wind in the spacecraft/shock frame. In contrast, they are propagating with the solar wind here; thus, they retain their intrinsic polarization.

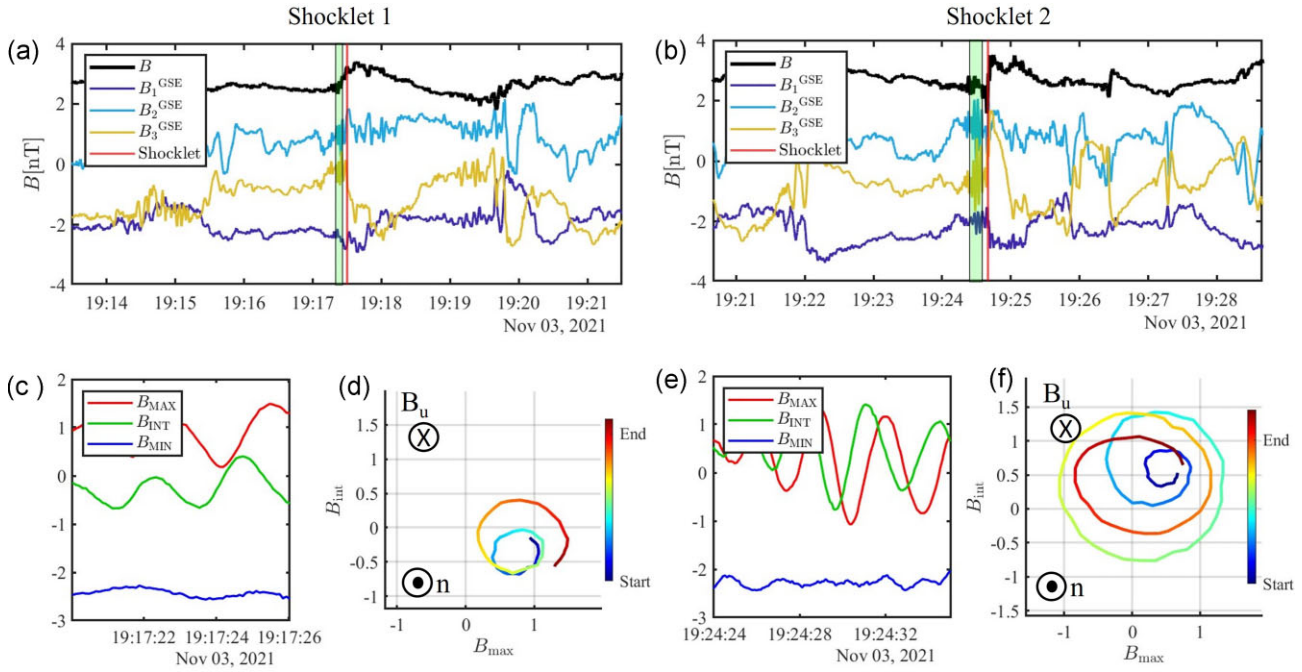

Figure 4. Panels (a)–(b): detailed view of the magnetic field around the upstream shocklets, identified by the vertical red line. The green shaded area indicates the whistler precursor. Panels (c)–(e): magnetic field components in the green shaded area, rotated to the minimum variance frame. Panels (d)–(f): magnetic field hodogram computed over the same time window, with the mean field and the MVA normal directions highlighted in the top and bottom left part of the plot, respectively.

3.3 Multi-spacecraft observations of shocklets

After a detailed characterization of the shocklets observed by the Wind spacecraft, we address the spatial and temporal behaviour of them using the other nearby spacecraft. Fig. 5 (left-hand panel) displays the magnetic field measurements of 5 spacecraft: ACE, DSCOVR, Wind, THEMIS-B, and THEMIS-C, respectively. All the spacecraft observe the IP shock passage (the times of crossing are reported in Table 1). The shocklet field, i.e. the portion of shock upstream filled with shocklets, is highlighted by the green shaded boxes. Here, it is possible to see that shocklet fields have been simultaneously observed at ACE, DSCOVR, and Wind, where the first two are upstream of Wind. It should be noted that, during the day analysed here, THEMIS B an C crossed the lunar wake (at times around 6 a.m. and 6 p.m., respectively). The grey shaded panel in Fig. 5 shows a portion of data from THEMIS C that may still be affected by the lunar wake.

To better understand the features of the upstream magnetic field for each L1 spacecraft, the measurements have been shifted in Fig. 5 (right-hand panel) such that the shock arrival is time is the same for each spacecraft (i.e. for each time-series, the transformation $t_{\rm Wind} = t + t_{\rm Shift}$, where $t_{\rm Shift}$ is the difference between the shock arrival time at each spacecraft and the shock arrival time at Wind). The vertical magenta line marks the shock transition time. The green shaded areas, show the shock upstream portion in which shocklets are observed. The shading scheme in the right-hand column is the same as the left-hand column of Fig. 5. The extent of these shocklet-filled portions of the shock upstream varies from ~ 8 to ~ 25 min. As it is evident from Fig. 5, shocklets appear to be persistent in the upstream upon its arrival at L1, but the finer details of their observations are extremely variable, possibly due to the rather small spatial and temporal scales (with respect to the inter spacecraft separations) characterizing the shocklets.

It is worth noting another feature visible in the shock upstream in Fig. 5, namely the magnetic field structure seen around 18:55 at Wind, present also in the DSCOVR and ACE time-series (see the blue shaded box in Fig. 5). The structure is characterized by a rise in field magnitude and a sharp change in the y–z components of the magnetic field. We note that no high-frequency precursor is observed here. As we can see in the Wind temperature profile in Fig. 3, this structure is also associated with a pre-heating of the incoming plasma. We speculate that the structure is probably a pre-existent solar wind feature ahead of the IP shock, due to the presence of another structure upstream of the shocklet field, visible between 19:05 and 19:12 Wind time at Wind and 19:10 to 19:25 Wind time at DSCOVR and highlighted by the purple panels in Fig. 5. Furthermore, the average field direction downstream of the structure suggests that it is not connected to the portion of the shock front observed by DSCOVR and Wind. A very interesting behaviour noted for such a structure is that it has a shorter duration at Wind, compared to DSCOVR, possibly an effect due to the fact that Wind is below the ecliptic plane (see the x–z plane in Fig. 6). Another explanation for this shorter duration is that it is due to a compression for which the shocklet field, likely populated with energetic particles, is responsible. Another explanation for this shortening could be related to the three-dimensional nature of the structure and the direction at which Wind and DSCOVR are crossing it. Such speculation need corroboration coming from particle data, out of scope for this work.

These simultaneous observations of upstream shocklets provide invaluable insights about their behaviour. First of all, combining the time-series observations with the spacecraft locations, it is possible to infer a size for the portion of space filled with shocklets, thus relating the information obtained from the time-series to a spatial information. Assuming a solar wind speed of 500 km s^{-1} (motivated by the Wind observations reported in Fig. 2), the L1 observations

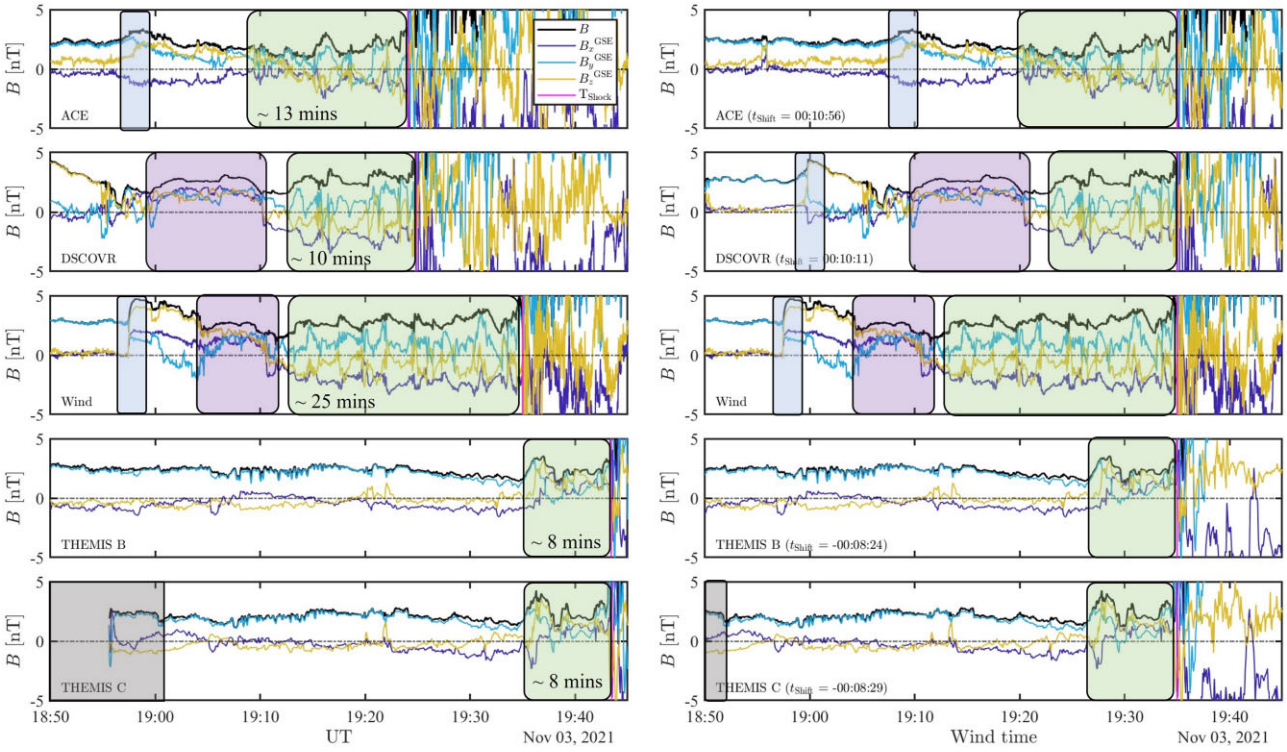

Figure 5. Left-hand panel: magnetic field overview of the shock arrival at several satellites around L1. From top to bottom are shown ACE, DSCOVR, Wind, THB, and THC. The magenta line marks the shock crossing time for each spacecraft. The green shaded boxes mark the shocklets filled shock upstream, and the duration of such intervals is specified on each box. The grey shaded box represents a portion of THEMIS C data stream that may be affected by the lunar wake. The orange and blue boxes indicate structures seen at multiple spacecraft discussed below. Right-hand panel: same as the left-hand panels, but where the observation time has been shifted such that the shock crossing time at each spacecraft corresponds to the time at which the IP shock crosses the Wind spacecraft.

reported in Fig. 5 have been used to assess the spatial portion of the IP shock upstream where shocklets are present.

Such an information is shown in the top two panels of Fig. 6. Here, the spacecraft positions at the time of the shock arrival at Wind are displayed in the x–y and x–z planes of the GSE coordinate system, together with the spatial region in which shocklets are observed (green shaded areas). The configuration is such that ACE and DSCOVR are the two most upstream satellites, THEMIS B and C are the two most downstream spacecraft. In Fig. 6, it is possible to observe the larger spread in the y-direction than the z-direction for the spacecraft group. Finally, the bottom panel of the Figure shows a three-dimensional overview of the spacecraft fleet in the GSE coordinate system, with the green shaded cylinders highlighting the shocklet field.

Neglecting shock curvature effects and considering the times in which DSCOVR and ACE simultaneously observe upstream shocklets, a lower limit for the extent of the shock front interacting with the upstream shocklets is about $71R_E$ (corresponding to ~ 2200 proton skin depths d_p using the average proton density upstream of Wind) in the x–y plane of the GSE coordinate system and $40R_E$ ($\sim 406d_p$) in the x–z plane, larger than the portion of the Earth's bow shock interacting with shocklets, being at most $30R_E$ (e.g. von Alfthan et al. 2014). With the same approach, we estimate a length for the upstream portion of space filled with shocklets using Wind observations. Again, assuming a solar wind speed of 500 km s^{-1}, the length of the upstream region filled the shocklets is at least $110R_E$ ($\sim 3500d_p$) long for the shock observed by Wind. Furthermore, the above results were projected in the shock normal frame using the shock normal vector computed at Wind, revealing that the shocklet field extends about $106R_E$ along the shock normal and $25R_E$ along the other two transverse directions.

4 CONCLUSIONS

In this work, we studied the interesting behaviour of a CME-driven IP shock observed near the Earth by ACE, DSCOVR, Wind, THEMIS B, and THEMIS C (in order of shock arrival time). We focused on the shock crossing at Wind, where *in situ* analyses show that the shock was quasi-parallel and characterized by high fast magnetosonic and Alfvenic Mach numbers, unusual for IP shocks. These parameters are consistent with the ones observed for the shock crossings at the other spacecraft (see Table 1). Upstream of this strong shock, we report very rare observations of shocklets, i.e. steep enhancements of magnetic field magnitude, with a typical time asymmetry between the rise and relaxation of the magnetic field signal. Using the Wind 3DP instrument, the presence of shocklets has been linked to an effective deceleration of the upstream plasma in the shock normal direction, thus highlighting their important role in pre-conditioning the incoming plasma for the shock transition. Performing a closer analysis of the shocklets, precursors of whistler waves have been identified in their upstream, a feature of their dispersive/transient nature. We note that the whistler precursor alone has been shown to affect the incident plasma (Chen et al. 2018; Hull et al. 2020; Wilson et al. 2009, 2017), and it is probably less influential than the entire shocklet structure, supporting the role of shocklets in the effective pre-conditioning of the upstream plasma.

Earlier in the day, at 14:04, the same shock was observed by Solar Orbiter at 0.81 AU from the Sun. Solar Orbiter was extremely well-

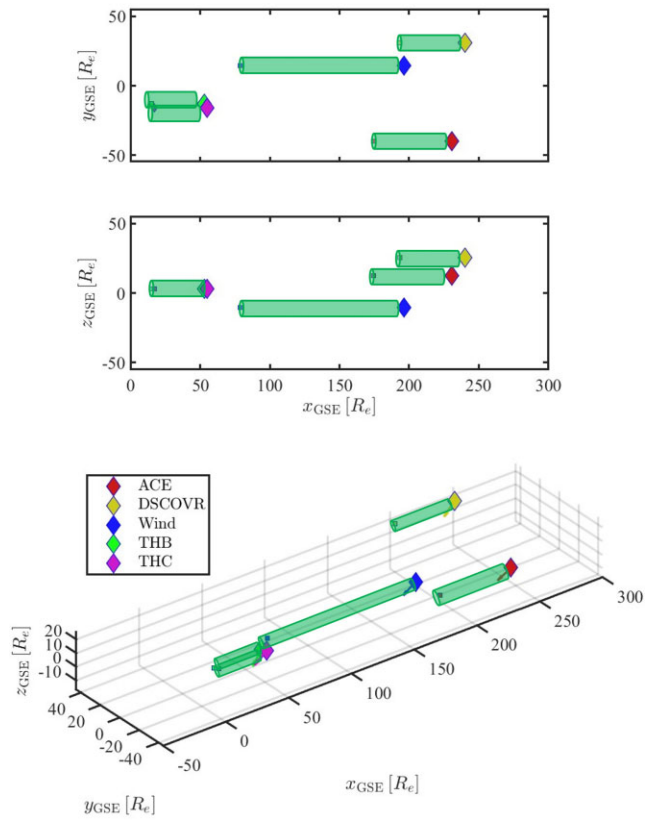

Figure 6. Top two panels: spacecraft positions in the GSE coordinate systems (diamonds) and portion of their upstream filled with shocklets (green arrows). Bottom panel: three-dimensional overview of spacecraft positions (diamonds). The colored arrows represent magnetic field measurements at Wind (blue) and THB (green), centred at the time of shock arrival at THB.

aligned to Earth, making it an excellent proxy to investigate the time history of this IP shock. At Solar Orbiter, the shock is estimated to have an oblique geometry ($\theta_{Bn} \sim 45^\circ$), and the shock parameter estimation is consistent with what observed at L1, namely high Mach number and shock speed. No shocklets were identified in the shock upstream at Solar Orbiter, probably due to the higher obliquity of the shock, together with the fact that the shock crossing happens in a very structured portion of the solar wind, due to the presence of magnetic structures both upstream and downstream, associated with changes in the plasma parameters. Another important ingredient is the shock time evolution: It is possible that the shock at Solar orbiter did not yet produce enough particles for efficient eave steepening upstream. We speculate that the higher shock obliquity, together with the structured nature of the shock upstream, creates unfavorable conditions for upstream waves to steepen and grow into shocklet structures.

However, observations of shocklets at IP shocks are extremely rare, with only two other cases reported in previous literature (Lucek & Balogh 1997; Wilson et al. 2009), probably due to the fact that usually IP shocks are not as strong as the one observed here, and shock strength is known to play an important role in the generation of different upstream ion populations (e.g. Savoini & Lembège 2015). For these reasons, our focus is on the shocklets observations at L1 and near-Earth where, for the first time, we use a multi-spacecraft approach to study these interesting structures.

Upstream shocklets have been found at each of the five spacecraft mentioned above. The upstream field filled with shocklets at these spacecraft highlights again the transient nature of these structures, with variable duration at each spacecraft, even in the presence of observations so close in time (see Fig. 5). The local shock obliquity estimates for this strong IP shock have a large range ($9^\circ \lesssim \theta_{Bn} \lesssim 64^\circ$), while at smaller planetary bow shocks shocklets are associated with quasi-parallel geometries. This spatial/temporal variation at a large-scale IP shock can offer an explanation for the previous surprising observation of shocklets at a similarly strong IP shock with local $\theta_{Bn} \sim 68^\circ$ by Wilson et al. (2009). This spacecraft configuration has also been used to address the portion of space filled with shocklets upstream of the IP shock, an important ingredient to consider when addressing several aspects of particle energization and energy conversion at strong shocks. Using ACE and DSCOVR observations, a lower limit for such portion of space has been estimated to be of about $71R_e$ in the x–y plane and $15R_e$ in the x–z plane for the transverse directions of the GSE coordinate system, and of at least $110R_E$ along the x GSE direction. These value correspond to about 2200, 406, and $3500d_p$, using the mean upstream proton density measured by the Wind spacecraft.

In a follow-up work, the relation between the presence of shocklets and the production of energetic particles away from the shock front, as well as a characterization of such structures from the point of view of scattering of suprathermal particles will be addressed, looking at the link between shock reflected particle distributions and mechanisms for wave steepening and shocklet formation. Under this point of view, it would be very interesting to study other strong IP shock events, that may become more common as we approach the solar maximum, using the capabilities of modern spacecraft such as Solar Orbiter, able to yield high-resolution measurements of energetic particles.

ACKNOWLEDGEMENTS

This work has received funding from the European Unions Horizon 2020 research and innovation programme under grant agreement No. 101004159 (SERPENTINE, www.serpentine-h2020.eu). DT is grateful to the SERPENTINE consortium for supporting this work. The work of HH is supported by the Royal Society award URF\R1\180671. HH thanks discussions in the ISSI International Team 465 'Foreshocks across the Heliosphere'. ND is grateful for support by the Turku Collegium for Science, Medicine and Technology of the University of Turku, Finland.

DATA AVAILABILITY

The Solar Orbiter data used in this study have been downloaded at soar.esac.esa.int. Data from all the other missions, used in this work, can be downloaded at https://cdaweb.gsfc.nasa.gov/.

REFERENCES

Andrés N., Gómez D., Bertucci C., Mazelle C., Dougherty M., 2013, Planet. Space Sci., 79-80, 64
Auster H. U. et al., 2008, Space Sci. Rev., 141, 235
Balogh A., Gonzalez-Esparza J. A., Forsyth R. J., Burton M. E., Goldstein B. E., Smith E. J., Bame S. J., 1995, Space Sci. Rev., 72, 171
Bertucci C., Achilleos N., Mazelle C., Hospodarsky G. B., Thomsen M., Dougherty M. K., Kurth W., 2007, J. Geophys. Res.: Space Phys., 112, A09219
Blanco-Cano X., Kajdic P., Aguilar-Rodríguez E., Russell C. T., Jian L. K., Luhmann J. G., 2016, J. Geophys. Res.: Space Phys., 121, 992
Burch J. L., Moore T. E., Torbert R. B., Giles B. L., Burch B. J. L., 2016, Space Sci Rev, 199, 5

Burgess D., Scholer M., 2015, Collisionless Shocks in Space Plasmas. Cambridge Univ. Press, Cambridge
Bykov A. M., Vazza F., Kropotina J. A., Levenfish K. P., Paerels F. B., 2019, Space Sci. Rev., 215, 1
Chen L.-J. et al., 2018, Phys. Rev. Lett., 120, 225101
Coates A. J., Mazelle C., Neubauer F. M., 1997, J. Geophys. Res.: Space Phys., 102, 7105
Dessler A. J., Fejer J. A., 1963, Planet. Space Sci., 11, 505
Dresing N., Theesen S., Klassen A., Heber B., 2016, A&A, 588, A17
Dungey J. W., 1979, Nuovo Cimento C Geophys. Space Phys. C, 2C, 655
Eastwood J. P., Hietala H., Toth G., Phan T. D., Fujimoto M., Toth G., Phan T. D., Fujimoto M., 2015, Space Sci Rev, 188, 251
Gieseler J. et al., 2022, preprint (arXiv:2210.00819)
Gosling J. T., Hildner E., MacQueen R. M., Munro R. H., Poland A. I., Ross C. L., 1974, J. Geophys. Res., 79, 4581
Guo F., Giacalone J., Zhao L., 2021, Frontiers Astron. Space Sci., 8, 27
Hellinger P., Mangeney A., Matthews A., 1996, Geophys. Res. Lett., 23, 621
Hoppe M. M., Russell C. T., 1982, Proc. Natl. Acad. Sci., 295, 236
Hoppe M. M., Russell C. T., 1983, J. Geophys. Res., 88, 2021
Hoppe M. M., Russell C. T., Frank L. A., Eastman T. E., Greenstadt E. W., 1981, J. Geophys. Res.: Space Phys., 86, 4471
Horbury T. S. et al., 2020, A&A, 642, A9
Hull A. J., Muschietti L., Le Contel O., Dorelli J. C., Lindqvist P.-A., 2020, J. Geophys. Res.: Space Phys., 125, e2019JA027290
Johlander A. et al., 2016, Phys. Rev. Lett., 117, 165101
Kajdič P., Preisser L., Blanco-Cano X., Burgess D., Trotta D., 2019, ApJ, 874, L13
Kennel C. F., Edmiston J. P., Hada T., 1985, Collisionless Shocks in the Heliosphere: A Tutorial Review. American Geophysical Union (AGU), Washington, DC
Kilpua E. K., Lumme E., Andreeova K., Isavnin A., Koskinen H. E., 2015, J. Geophys. Res.: Space Phys., 120, 4112
Kilpua E., Koskinen H. E. J., Pulkkinen T. I., 2017, Living Rev. Sol. Phys., 14, 5
Kivelson M., Russell C., 1995, Introduction to Space Physics. Cambridge Univ. Press, Cambridge
Koval A., Szabo A., 2008, J. Geophys. Res.: Space Phys., 113, A10110
Le G., Russell C. T., Thomsen M. F., Gosling J. T., 1992, J. Geophys. Res.: Space Phys., 97, 2917
Lepping R. P. et al., 1995, Space Sci. Rev., 71, 207
Lin R. P. et al., 1995, Space Sci. Rev., 71, 125
Lucek E. A. et al., 2002, Ann. Geophys., 20, 1699
Lucek E. A., Balogh A., 1997, Geophys. Res. Lett., 24, 2387
Lucek E. A., Horbury T. S., Dandouras I., Rème H., 2008, J. Geophys. Res.: Space Phys., 113, A07S02
McFadden J. P. et al., 2008, Space Sci. Rev., 141, 277
Naeem I., Ehsan Z., Mirza A. M., Murtaza G., 2020, Phys. Plasmas, 27, 043703
Nakanotani M., Zank G. P., Zhao L.-L., 2022, ApJ, 926, 109
Ogilvie K. W. et al., 1995, Space Sci. Rev., 71, 55
Omidi N., Winske D., 1990, J. Geophys. Res.: Space Phys., 95, 2281
Owen C. J. et al., 2020, A&A, 642, A16
Paschmann G., Schwartz S. J., 2000, in Harris R. A., ed., ESA-SP, Vol. 449, Cluster-II Workshop Multiscale/Multipoint Plasma Measurements. AG Noordwijk, The Netherlands, p. 99
Plaschke F. et al., 2018, Space Sci. Rev., 214, 81
Preisser L., Blanco-Cano X., Kajdic P., Burgess D., Trotta D., 2020, ApJ Lett., 900, L6
Reames D. V., 1999, Space Sci. Rev., 90, 413
Richardson I. G., 2018, Living Rev. Sol. Phys., 15, 1
Russell C. T., Childers D. D., Coleman P. J. Jr, 1971, J. Geophys. Res., 76, 845
Savoini P., Lembège B., 2015, J. Geophys. Res.: Space Phys., 120, 7154
Scholer M., Kucharek H., Shinohara I., 2003, J. Geophys. Res. (Space Phys.), 108, 1273
Smith C. W., L'Heureux J., Ness N. F., Acuña M. H., Burlaga L. F., Scheifele J., 1998, Space Sci. Rev., 86, 613
Stasiewicz K., Eliasson B., Cohen I. J., Turner D. L., Ergun R. E., 2021, J. Geophys. Res.: Space Phys., 126, e2021JA029477
Stasiewicz K., Klos Z., 2022, MNRAS, 513, 5892
Stasiewicz K., Longmore M., Buchert S., Shukla P. K., Lavraud B., Pickett J., 2003, Geophys. Res. Lett., 30, 2241
Szabo A., Koval A., Kasper J. C., Stevens M., Case A., Biesecker D., Reinard A., Cash M., 2016, Solar Heliospheric and INterplanetary Environment (SHINE 2016). Santa Fe, NM, p. 9
Thomsen M. F., Bame S. J., Feldman W. C., Gosling J. T., McComas D. J., Young D. T., 1986, Geophys. Res. Lett., 13, 393
Trotta D. et al., 2022a, Frontiers Astron. Space Sci., 9, available at: https://doi.org/10.3389/fspas.2022.1005672
Trotta D. et al., 2022b, ApJ, 933, 167
Trotta D., Burgess D., 2018, MNRAS, 482, 1154
Trotta D., Valentini F., Burgess D., Servidio S., 2021, Proc, Natl. Acad. Sci., 118, e2026764118
Tsurutani B. T., Southwood D. J., Smith E. J., Balogh A., 1993, J. Geophys. Res.: Space Phys., 98, 21203
Tsurutani B. T., Thorne R. M., Smith E. J., Gosling J. T., Matsumoto H., 1987, J. Geophys. Res.: Space Phys., 92, 11074
von Alfthan S., Pokhotelov D., Kempf Y., Hoilijoki S., Honkonen I., Sandroos A., Palmroth M., 2014, J. Atmos. Sol.-Terr. Phys., 120, 24
Wilson L. B. I., Cattell C. A., Kellogg P. J., Goetz K., Kersten K., Kasper J. C., Szabo A., Meziane K., 2009, J. Geophys. Res.: Space Phys., 114, A10106
Wilson L. B. III, 2016, Low Frequency Waves at and Upstream of Collisionless Shocks. American Geophysical Union (AGU), Washington, DC
Wilson L. B. III, et al., 2013, J. Geophys. Res.: Space Phys., 118, 957
Wilson L. B. III, et al., 2021, Rev. Geophys., 59, e2020RG000714
Wilson L. B. III, Koval A., Szabo A., Stevens M. L., Kasper J. C., Cattell C. A., Krasnoselskikh V. V., 2017, J. Geophys. Res.: Space Phys., 122, 9115

This paper has been typeset from a TEX/LATEX file prepared by the author.